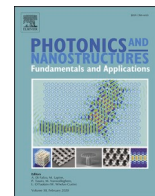




Contents lists available at ScienceDirect

Photonics and Nanostructures - Fundamentals and Applications

journal homepage: www.elsevier.com/locate/photonics

Multi-focusing metalenses based on quadrangular frustum pyramid-shaped nanoantennas

Shaoguang Zhao^a, Yiqing Wang^a, Zheng-Da Hu^a, Aliaksei Balmakou^c, Sergei Khakhomov^c, Igor Semchenko^c, Jicheng Wang^{a,b,*}

^a School of Science, Jiangsu Provincial Research Center of Light Industrial Optoelectronic Engineering and Technology, Jiangnan University, Wuxi 214122, China

^b State Key Laboratory of Applied Optics, Changchun Institute of Optics, Fine Mechanics and Physics, Chinese Academy of Sciences, Changchun 130033, China

^c Departments of Optics, Francisk Skorina Gomel State University, Gomel 246019, Belarus

ARTICLE INFO

Keywords:

Metalens
Metamaterials
Multi-focusing
Silicon
Nanoantennas

ABSTRACT

This paper presents ultrathin multi-focusing metalenses that can produce several independent focusing spots, useful in imaging for light flow redistribution, even asymmetrical into many focal spots. The proposed design includes quadrangular frustum pyramids serving as individually tuned nanoantennas; their structure can be modified, facilitating wave-phase retardation tuning. Combining the propagation phase control with the Pancharatnam-Berry phase principle allows the screening of various cell structures. The specific design of the unit-cell structures makes the metalenses capable of single- and double-focusing at the required focal length. Thus, this metalens design might help in developing precision optics for micro-object manipulation.

Data Availability: The data that support the findings of this study are available from the corresponding author upon reasonable request.

Recent advances in metamaterials have attracted growing interest from the scientific and engineering community worldwide [1–4]. One of the fascinating intrinsic features of metamaterials is their ultrathin thickness, which distinguishes them from traditional, natural materials [5]. The subwavelength thinness of some metamaterials has led to the creation of a subclass of so-called metasurfaces, which are capable of shaping the light phase, amplitude, and polarization; this ability has been effectively used to design ultrathin focusing lenses called metalenses [6,7]. Metalenses have extremely wide applicability since they can not only replace but also overcome the functionalities of traditional optical lenses, e.g., by breaking through the diffraction limit [8]. Compared with traditional lenses, metalenses present the following advantages: light weight, small thickness and volume, suitability for mass production, and absence of the diffraction limit. Hence, metalenses are applicable in both new and existing technologies, including beam refraction [9,10], achromatic optics [11,12], light focusing [13–15], vortex beam modulation [8,16], ultra-resolution and holographic imaging [17–21], and image coding [22,23].

In the metalens design, using metals is privileged [24,25]; however, this leads to high energy losses and temperature instability. Thus,

designing metalenses with reduced energy losses using high-refractive-index nonmetallic constituents, which do not deteriorate their high transmittance or limit their manufacturability, is a current challenge [26–29]. Recently, there have been various attempts for topologically optimizing metalenses. For instance, Yueshen et al. [30] proposed the use of conical structures to modify the metalens surface; however, the conical structures are conjugated and there are some difficulties in controlling their high-precision angularity during manufacturing. Li et al. [31] used a quadrangular prism nano-antenna to achieve subdiffraction focusing. However, this work did not make full use of the abundant structural parameters of the quadrangular prism nano-antenna. They only changed the rotation angle of the nano-antenna to realize full phase control.

In the present study, quadrangular frustum pyramid-shaped structures were used to modify metalenses while maintaining a transmittance comparable with traditional lenses. These structures have many parameters that can be adjusted for phase modulation; they were also selected because of their successful utilization in manufacturing facilities [32,33]. The pyramids used in the metalenses were topologically optimized by combining the Pancharatnam-Berry (PB) phase principle

* Corresponding author at: School of Science, Jiangsu Provincial Research Center of Light Industrial Optoelectronic Engineering and Technology, Jiangnan University, Wuxi 214122, China.

E-mail address: jcwang@jiangnan.edu.cn (J. Wang).

<https://doi.org/10.1016/j.photonics.2021.100957>

Received 30 December 2020; Received in revised form 21 July 2021; Accepted 16 August 2021

Available online 19 August 2021

1569-4410/© 2021 Elsevier B.V. All rights reserved.

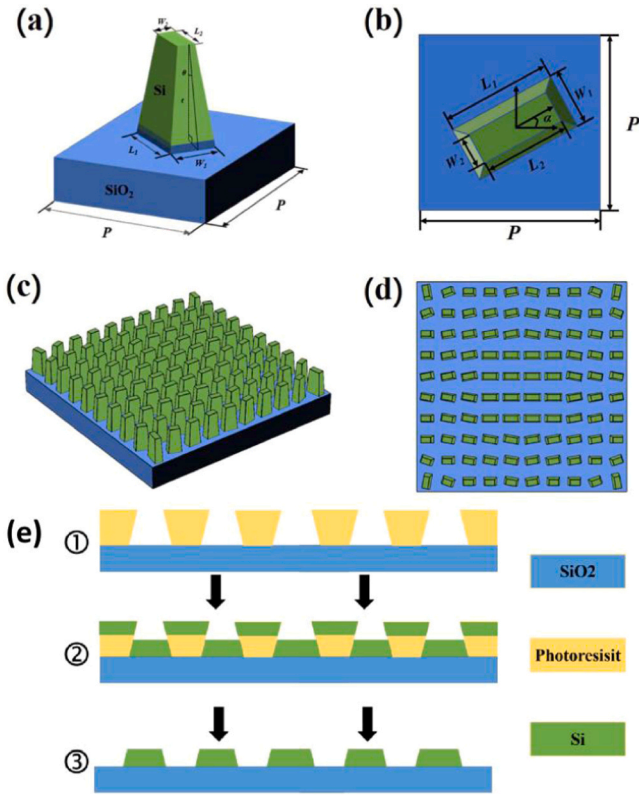


Fig. 1. Design of the metalens: (a) unit-cell and (b) its top view, with the structural parameters indicated; (c) lateral and (d) top views of the whole metalens. (e) Manufacturing flow chart: (1) pattern of the photoresist, (2) E-beam evaporation of Si film, and (3) removing the photoresist.

[34] with phase retardation analysis [35]. The cell structures were screened to find those capable of producing phase changes in the 2π range; noticeably, when using the selected pyramidal structures, both single- and double-focusing arrays could be designed. Additionally, simulations demonstrated that the designed arrays can produce perfect focusing effects.

The usage of Si pyramidal structures periodically distributed onto a SiO₂ substrate allows significant metasurface modifications and topological optimization with reduced dissipative losses; Si provides a high refractive-index contrast between the building blocks, represented by subwavelength Si truncated pyramids and the air. The pyramids are considered as waveguides of a Fabry–Perot resonator, i.e., they have a low-quality factor, necessary for high transmittance. Compared with the

traditional cuboid structure [36–38], the pyramidal structure is more versatile in terms of structural modification, which enables fine wave-phase retardation tuning.

The metalenses were prototyped and optimized for being excited by an incident linearly polarized light at the resonant wavelength of 1550 nm. Then, variational analysis and topological optimization were performed using the finite-element solver COMSOL Multiphysics (Fig. 1). We set periodic boundary conditions in the x and y directions to simulate the situation of infinite periodic arrays. A perfect matching layer was set in the z direction to perfectly absorb scattered stray light and prevent it influencing the simulation results. The grid size was optimized to one-fifth of the incident wavelength, making the simulation results more accurate. The metalens arrays consisted of 12 building blocks (or meta-atoms), which acted as individual subunits with specific phase retardation characteristics covering a phase interval of $\pi/6$ for each block; the 12 cell structures could produce phase shift changes in the 2π range. According to the PB phase principle, when determining the phase retardation, the rotation angle (α) (Fig. 1b) was considered a primary variable, and the secondary variables [e.g., the dip angle of the platform (θ), the side length of the upper and lower bottom sides of the platform ($L_{1,2}$ and $W_{1,2}$, respectively), the height of the platform (t), and the array periodicity, i.e., the period of the unit-cell (P)], dependent on the primary ones, were tuned during the variational analysis. In particular, the combination of L_1 and α allowed full-range phase variability (2π) and high transmittance. Finally, the invariant structural parameters, such as θ and $W_{1,2}$, were independently optimized to finely tune the transmittance. The design process flow of the metasurface is shown in Fig. 1e.

When the resonant incident wavelength was 1550 nm, the unit-cell parameters were optimized as follows: $P = 700$ nm, $W_1 = 250$ nm, $\theta = 1.5^\circ$, $t = 820$ nm, $W_2 = W_1 - 2t \tan(\theta)$, and $L_2 = L_1 - 2t \tan(\theta)$. Fig. 2 displays the phase retardation and transmittance diagrams for all the variety of unit-cell rotation positioning obtained when changing α simultaneously with L_1 , which are also summarized in Table 1.

The wave-phase retardation depends on the prism shape and orientation (Fig. 2a). The phase and transmittance changes of the 12 unit-cells are shown in Fig. 3a, and the resulting transmittance was 0.8 or more for all the cases. When the light propagated through a one-dimensional (1D) array composed of all the 12 orientations (Fig. 3a), it was deflected by 9.6° (Fig. 3b). According to generalized Snell's law, the deflection angle (α_t) can be expressed as follows:

$$n_t \sin \alpha_t - n_i \sin \alpha_i = \frac{\lambda}{2\pi} \frac{d\phi(x)}{dx}, \quad (1)$$

where $\alpha_i = 0$ is the angle of the incident light, n_i is the refractive index of the incident medium, and n_t is the refractive index of the propagating medium. The calculated α_t value was approximately $\sin^{-1}(\lambda/12P)$

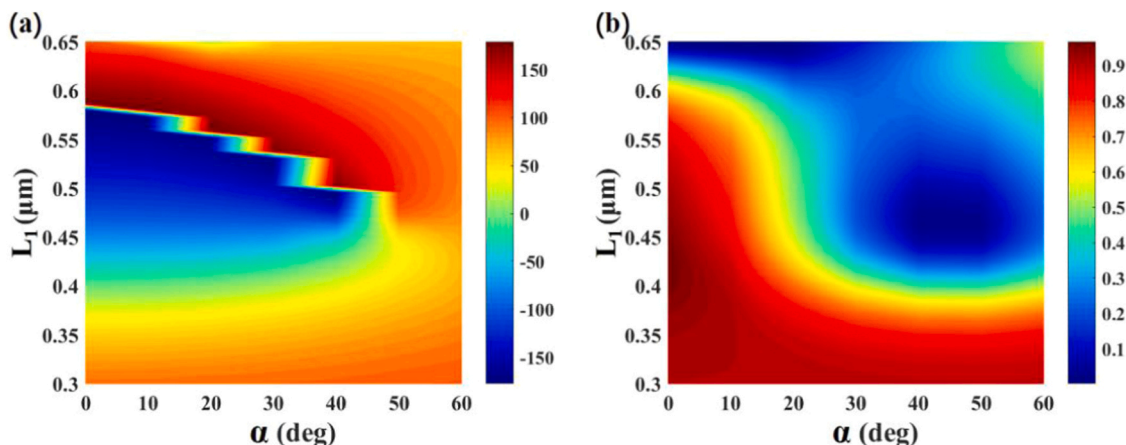


Fig. 2. (a) Phase retardation and (b) transmittance diagrams of the full variety of unit-cell rotational positioning.

Table 1Phase retardation (Phase) and L_1 (length of the longer bottom sides of the platform) for all 12 unit-cell rotation angles (α).

Phase ($^\circ$)	-165	-135	-105	-75	-45	-15	15	45	75	105	135	165
α ($^\circ$)	0	10	10	10	0	20	20	40	60	0	0	0
L_1 (nm)	559	510	475	447	426	412	391	384	384	650	629	601

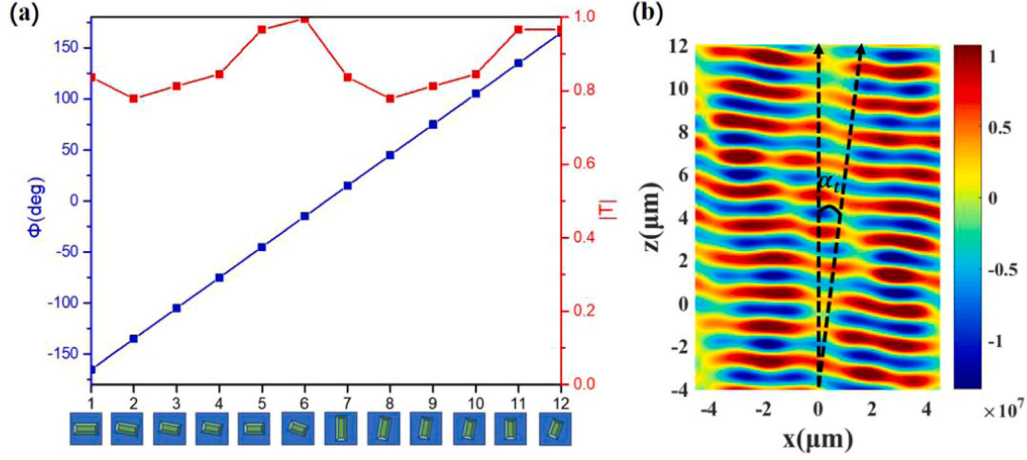


Fig. 3. (a) Wave-phase retardation and transmittance as a function of the orientation of the pyramidal unit-cells when light propagates through each of them. (b) Optical deflection of light (9.6°) when propagating through a one-dimensional array composed of all the orientations of the 12 unit-cells shown in (a).

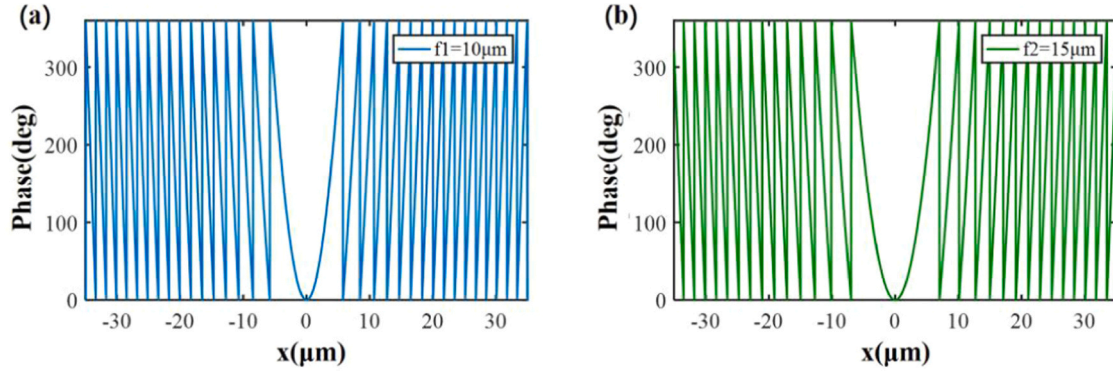


Fig. 4. Phase distribution of the one-dimensional single-focusing array for different focal lengths: (a) 10 and (b) 15 μm .

$= 10.63^\circ$.

A 1D array design for single- and multi-focusing is presented here: it can realize single-focusing in different positions and double-focusing in the z and x directions (the array plane is put on the xy plane).

According to the principle of equal optical path and the phase control mechanism, the phase distribution of the single-focusing 1D array can be expressed as follows [38]:

$$\phi(x) = 2\pi/\lambda \left(\sqrt{x^2 + f^2} - |f| \right) - 2n\pi, \quad (2)$$

where λ is the wavelength of the incident light, x is the distance from each position in the array to the central origin, f is the focal length, and n is an integer. The as-calculated phase distribution, obtained for two f values ($f_1 = 10 \mu\text{m}$ and $f_2 = 15 \mu\text{m}$), is plotted in Fig. 4.

The 1D array structure was designed to evaluate the focusing performance of the arrays (Fig. 4). Thus, 1D focusing arrays with flexibly adjusted focal lengths in the 10–25 μm range were designed. The quality of focusing localization and the focal spot shape depended on the focal length. With increasing focal length, the full width at half maximum (FWHM) of the intensity at the focal point decreased from 1.18 to

0.86 μm ; i.e., the focusing localization increased, although the focusing depth elongated along the z axis. The numerical aperture, expressed as $NA = \sin[\tan^{-1}(D/2f)]$, where D is the array diameter of the, was calculated for the following designed lenses: $NA_1 = 0.962$, $NA_2 = 0.917$, $NA_3 = 0.868$, and $NA_4 = 0.8137$. Fig. 5.

Multi-focusing lenses can be realized with a 1D array if the array structure is rearranged for the desired phase distribution and the focus localization along the x axis is governed by the following expression:

$$\phi(x) = \begin{cases} 2\pi/\lambda \left(\sqrt{x^2 + f_1^2} - |f_1| \right) - 2n\pi & -D/2 \leq x < 0 \\ 2\pi/\lambda \left(\sqrt{x^2 + f_2^2} - |f_2| \right) - 2n\pi & 0 < x \leq D/2 \end{cases} \quad (3)$$

The distance between the two focal points along the x axis could be controlled, as well as the focus positioning. Eq. (3) indicates that the double-focusing focus arrays are composed of two single-focusing focus arrays. The focusing effect shown in Fig. 6a and b suggests that the two focus focusing effects are perfect and do not interfere with each other; this result provides a train of thought for the study of a multi-focusing metalens. The FWHM values obtained under illumination by linearly polarized light (1550 nm) along the x axis are shown in Fig. 6c and d.

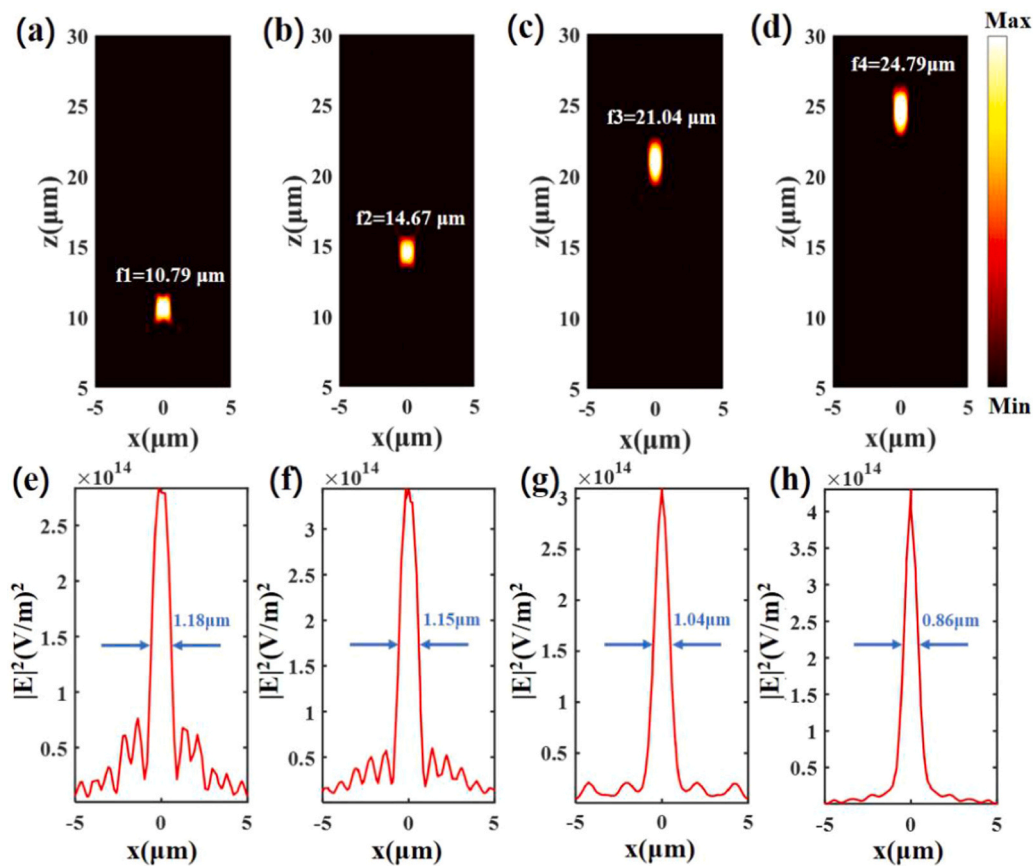


Fig. 5. (a–d) Focus localization and (e–h) axial intensity distribution for the different focal lengths: 10.79 (a, e), 14.67 (b, f), 21.04 (c, g), and 24.79 μm (d, h). In (e–h), the arrows indicate the full width at half maximum.

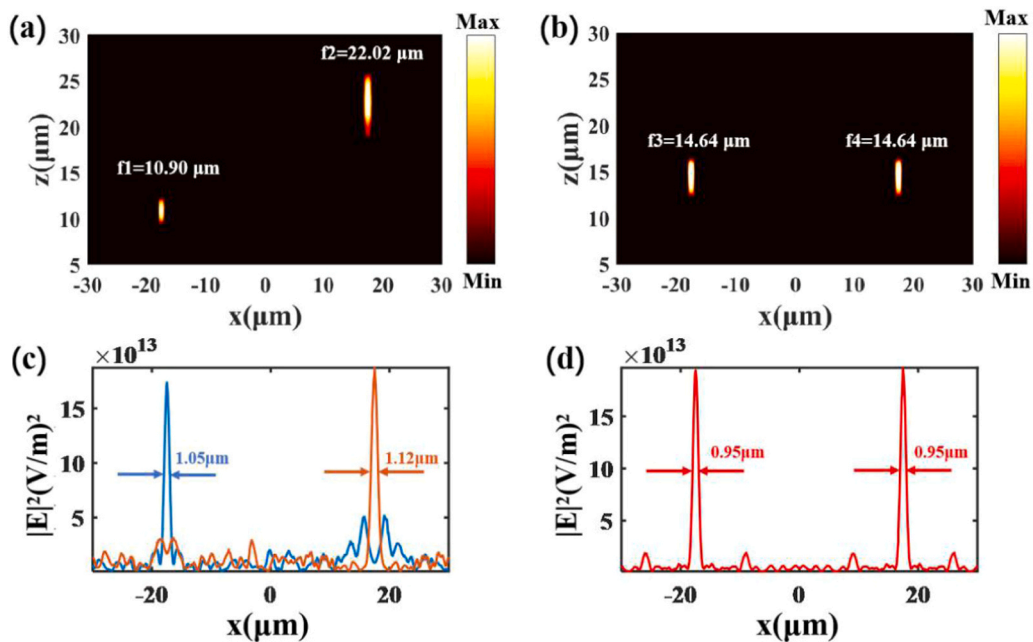


Fig. 6. Realization of double-focusing with (a) xy plane delocalization and (b) in xy plane localization. (c, d) Corresponding intensity distributions and full width at half maximum at the focal lengths (f) indicated in (a, b).

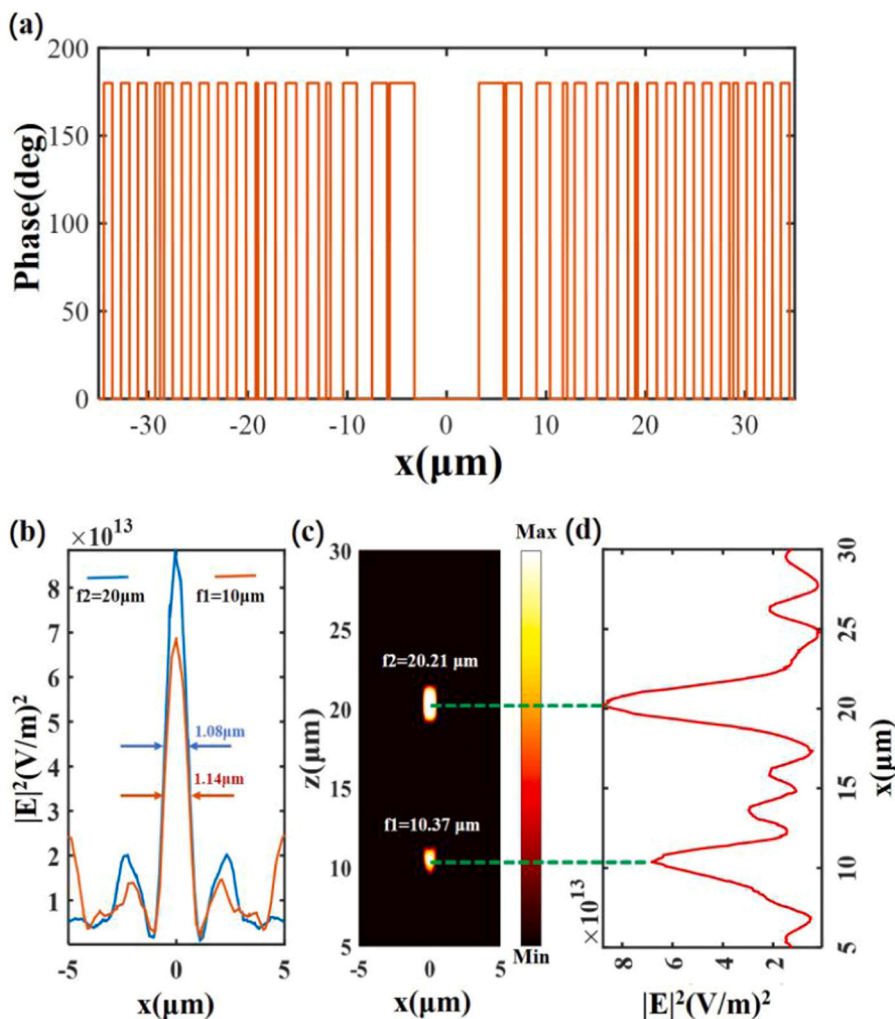


Fig. 7. (a) Phase distribution along the x axis for the double-focusing one-dimensional array. (b) The intensity of focus ($|E|^2$) measured at two focal lengths (f), along with the corresponding full width at half maximum. (c) Visualization of the incident light focusing on the two focal points along the z axis. (d) Intensity of focus measured along the z axis when $x = 0$.

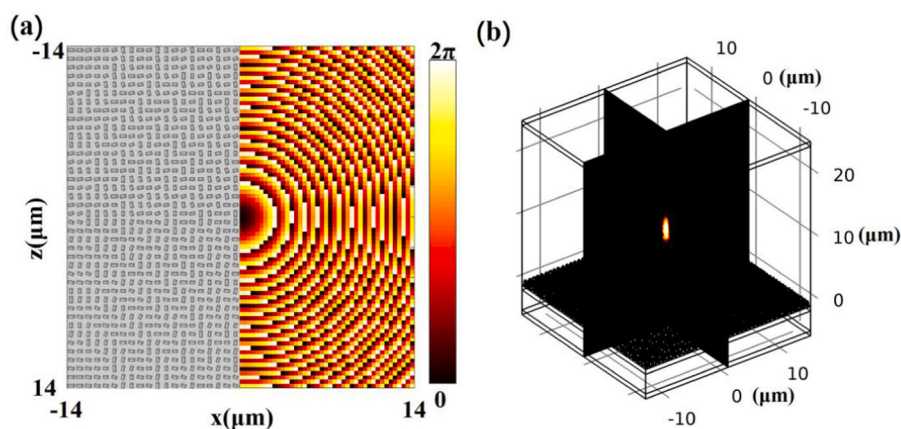


Fig. 8. (a) Top view of the two-dimensional metalens and the corresponding phase distribution for single-focusing. (b) Visualization of the focusing effect at a focal length of 10.79 μm .

The phase distribution for multi-focusing when the focal spots are delocalized in a xy plane can be expressed as follows:

$$\Phi_L(x) = \arg\{\exp[i(\phi_1(x))] + \exp[i(-\phi_1(x))] + \exp[i(\phi_2(x))] + \exp[i(-\phi_2(x))]\}, \quad (4)$$

where $\phi_1(x)$ and $\phi_2(x)$ control the positions of f_1 and f_2 , respectively. $\phi(x)$ is determined by Eq. (2), and the distance between two focal points along the z axis can be expressed as $d = |f_1 - f_2|$. Fig. 7 illustrates the phase distribution and performance for the double-focusing 1D array.

Table 2
Comparison with other studies.

Wavelength	NA	Polarization	Function	Focal length	Transmittance	Material
0.86 THz	0.2	Linear	Multi-focusing	2–5 mm	~0.7	Gold[39]
632.8 nm	0.74	Linear	Multi-focusing	5–11 μm	~0.6	Gold[15]
480 nm	0.65	TE/TM	Multi-focusing	8–14 μm	~0.9	TiO ₂ [27]
1550 nm	0.982	Circular	Single-focusing	4–5 μm	~0.95	Si[31]
1550 nm	0.8–0.96	Linear	Multi-focusing	10–25 μm	~0.95	Si (our work)

The simulation of the 1D array demonstrated the feasibility of a focusing metalens, but had limited practical applications. However, the results can be used as a reference for designing more complex systems. For example, the phase distribution of a 2D array can be expressed as follows:

$$\phi(x, y) = 2\pi/\lambda \left(\sqrt{R^2 + f^2} - |f| \right) - 2n\pi, \quad (5)$$

where $R = (x^2 + y^2)^{1/2}$ is the distance from any point on the 2D plane to its origin.

Such a 2D array was designed by placing 40×40 unit-cells on a SiO₂ substrate; each element corresponded to the phase requirements shown in Fig. 8a. Fig. 8b shows the ability of this metalens to focus the impinging radiation at a focal length of 10.79 μm , which is close to the theoretically calculated value of 10 μm .

Finally, we compared our work with other recent metalens work in Table 2. Compared to metal metalenses, dielectric metalenses can obtain higher transmittance (Table 2). Our work has a larger NA compared to other multi-focal focusing metalenses.

Analytical calculations and modern numerical simulations were combined to design and evaluate an array composed of Si pyramids capable of driving light in an intriguing nontrivial manner. First, the underlying principles of beam deflection were outlined; then, the basic physical mechanisms of the in- and out-of-plane focusing in 1D configuration, as a base for the more complex 2D metalenses, were demonstrated. The numerical simulations showed that, when properly configuring the structural parameters of the basic blocks (i.e., their spatial arrangement, periodicity pattern, material parameters, and array dimensions), monochromatic light can be efficiently focused at the desired focal length. An additional multi-focusing compatibility claimed the metalens functionality beyond the reach of traditional technologies. Such metalenses can be fabricated at existing production sites via the traditional Si formation technology. The ultrathin design of metalenses can extend their applications, strictly subject to space limitations, in various technological fields, including terahertz imaging.

Declaration of Competing Interest

The authors declare that they have no known competing financial interests or personal relationships that could have appeared to influence the work reported in this paper.

Acknowledgments

This work was supported in part by the National Natural Science Foundation of China (11811530052), Intergovernmental Science and Technology Regular Meeting Exchange Project of Ministry of Science and Technology of China (CB02-20), Open Fund of State Key Laboratory of Applied Optics (SKLAO2020001A04), and Graduate Research and Innovation Projects of Jiangsu Province (SJCX20_0763).

References

- [1] J.B. Pendry, A.J. Holden, D.J. Robbins, W.J. Stewart, Magnetism from conductors and enhanced nonlinear phenomena, *IEEE Trans. Microw. Theory Technol.* 47 (1999) 2075–2084.
- [2] C.M. Soukoulis, M. Wegener, Past achievements and future challenges in the development of three-dimensional photonic metamaterials, *Nat. Photon.* 5 (2011) 523–530.
- [3] J.B. Pendry, A.J. Holden, W.J. Stewart, I. Youngs, Extremely low frequency plasmons in metallic mesostructures, *Phys. Rev. Lett.* 76 (1996) 4773–4776.
- [4] D.R. Smith, W.J. Padilla, D.C. Vier, S.C. Nemat-Nasser, S. Schultz, Composite medium with simultaneously negative permeability and permittivity, *Phys. Rev. Lett.* 84 (2000) 4184–4187.
- [5] N. Yu, P. Genevet, M.A. Kats, F. Aieta, J.P. Tetienne, F. Capasso, Z. Gaburro, Light propagation with phase discontinuities: generalized laws of reflection and refraction, *Science* 334 (2011) 333–337.
- [6] Y. Hu, X. Wang, X. Luo, X. Ou, L. Li, Y. Chen, S. Wang, H. Duan, Y. Ping, All-dielectric metasurfaces for polarization manipulation: principles and emerging applications, *Nanophotonics* 9 (2020) 3755–3780.
- [7] L. Li, Z. Liu, X. Ren, S. Wang, V. Su, M. Chen, C.H. Chu, H.Y. Kuo, B. Liu, W. Zang, G. Guo, L. Zhang, Z. Wang, S. Zhu, D.P. Tsai, Metalens-array-based high-dimensional and multiphoton quantum source, *Science* 368 (2020) 1487–1490.
- [8] K. Zhang, Y. Yuan, D. Zhang, X. Ding, B. Ratni, S.N. Burokur, M. Lu, K. Tang, Q. Wu, Phase-engineered metalenses to generate converging and non-diffractive vortex beam carrying orbital angular momentum in microwave region, *Opt. Express* 26 (2018) 1351–1360.
- [9] F. Aieta, P. Genevet, N. Yu, M.A. Kats, Z. Gaburro, F. Capasso, Out-of-plane reflection and refraction of light by anisotropic optical antenna metasurfaces with phase discontinuities, *Nano Lett.* 12 (2012) 1702–1706.
- [10] Y. Yuan, K. Zhang, X. Ding, B. Ratni, S.N. Burokur, Q. Wu, Complementary transmissive ultra-thin meta-deflectors for broadband polarization-independent reflections in the microwave region, *Photon. Rev.* 7 (2019) 80–88.
- [11] R.J. Lin, V. Su, S. Wang, M.K. Chen, T.L. Chung, Y.H. Chen, H.Y. Kuo, J. Chen, J. Chen, Y. Huang, J. Wang, C.H. Chu, P.C. Wu, T. Li, Z. Wang, S. Zhu, D.P. Tsai, Achromatic metalens array for full-colour light-field imaging, *Nat. Nanotechnol.* 14 (2019) 227–231.
- [12] H. Zhou, L. Chen, F. Shen, K. Guo, Z. Guo, Broadband achromatic metalens in the midinfrared range, *Phys. Rev. Appl.* 11 (2019), 024066.
- [13] C. Chen, W. Song, J. Chen, J. Wang, Y.H. Chen, B. Xu, M. Chen, H. Li, B. Fang, J. Chen, H.Y. Kuo, S. Wang, D.P. Tsai, S. Zhu, T. Li, Spectral tomographic imaging with aplanatic metalens, *Light Sci. Appl.* 8 (2019) 99.
- [14] L. Ma, J. Guan, Y. Wang, C. Chen, J. Zhang, J. Lin, J. Tan, P. Jin, Diffraction-limited axial double foci and optical traps generated by optimization-free planar lens, *Nanophotonics* 9 (2020) 841–853.
- [15] H. Shao, C. Chen, J. Wang, L. Pan, T. Sang, Metalenses based on the non-parallel double-slit arrays, *J. Phys. D* 50 (2017), 384001.
- [16] W. Wang, C. Guo, J. Tang, Z. Zhao, J. Wang, J. Sun, F. Shen, K. Guo, Z. Guo, High-efficiency and broadband near-infrared bi-functional metasurface based on rotary different-size silicon nanobricks, *Nanomaterials* 9 (2019) 1744.
- [17] J. Chen, T. Li, S. Wang, S. Zhu, Multiplexed holograms by surface plasmon propagation and polarized scattering, *Nano Lett.* 17 (2017) 5051–5055.
- [18] J. Deng, Z. Li, G. Zheng, J. Tao, Q. Dai, L. Deng, P.A. He, Q. Deng, Q. Mao, Depth perception based 3D holograms enabled with polarization-independent metasurfaces, *Opt. Express* 26 (2018) 11843–11849.
- [19] Y. Hu, L. Li, Y. Wang, M. Meng, L. Jin, X. Luo, Y. Chen, X. Li, S. Xiao, H. Wang, Y. Luo, C. Qiu, H. Duan, Trichromatic and tripolarization-channel holography with noninterleaved dielectric metasurface, *Nano Lett.* 20 (2019) 994–1002.
- [20] M. Khorasaninejad, W.T. Chen, R.C. Devlin, J. Oh, A.Y. Zhu, F. Capasso, Metalenses at visible wavelengths: diffraction-limited focusing and subwavelength resolution imaging, *Science* 352 (2016) 1190–1194.
- [21] H. Zhou, B. Sain, Y. Wang, C. Schlickriede, R. Zhao, X. Zhang, Q. Wei, X. Li, L. Huang, T. Zentgraf, Polarization-encrypted orbital angular momentum multiplexed metasurface holography, *ACS Nano* 14 (2020) 5553–5559.
- [22] J. Wu, J. Wang, Y. Nie, L. Hu, Multiple-image optical encryption based on phase retrieval algorithm and fractional Talbot effect, *Opt. Express* 27 (2019) 35096–35106.
- [23] H. Zhao, C. Zhang, J. Guo, S. Liu, X. Chen, Y. Zhang, Adhesive-layer-free and double-faced nanotransfer lithography for a flexible large-area metasurface hologram, *ACS Appl. Mater. Interfaces* 12 (2020) 1737–1745.
- [24] H. Li, G. Wang, T. Cai, H. Hou, W. Guo, Wideband transparent beam-forming metadevice with amplitude- and phase-controlled metasurface, *Phys. Rev. Appl.* 11 (2019), 014043.
- [25] X. Song, L. Huang, L. Sun, X. Zhang, R. Zhao, X. Li, J. Wang, B. Bai, Y. Wang, Near-field plasmonic beam engineering with complex amplitude modulation based on metasurface, *Appl. Phys. Lett.* 112 (2018), 073104.
- [26] D. Lin, P. Fan, E. Hasman, M.L. Brongersma, Dielectric gradient metasurface optical elements, *Science* 345 (2014) 298–302.
- [27] R. Lin, X. Li, Multifocal metalens based on multilayer Pancharatnam-Berry phase elements architecture, *Opt. Lett.* 44 (2019) 2819–2822.

- [28] Z. Ma, Y. Li, Y. Li, Y. Gong, S.A. Maier, M. Hong, All-dielectric planar chiral metasurface with gradient geometric phase, *Opt. Express* 26 (2018) 6067–6078.
- [29] F. Zhang, H. Yu, J. Fang, M. Zhang, S. Chen, J. Wang, A. He, J. Chen, Efficient generation and tight focusing of radially polarized beam from linearly polarized beam with all-dielectric metasurface, *Opt. Express* 24 (2016) 6656–6664.
- [30] Y. Shen, X. Luo, Efficient bending and focusing of light beam with all-dielectric subwavelength structures, *Opt. Commun.* 366 (2016) 174–178.
- [31] H. Li, Q. Zhang, X. Jiang, G. Liang, Z. Wen, Z. Zhang, Z. Shang, G. Chen, Subdiffraction focusing lens based on quadrangular-frustum pyramid-shaped metasurface, *Appl. Opt.* 58 (2019) 7688–7692.
- [32] H. Yang, H. Liu, B. Song, Y. Li, D. Meng, B. Chen, P. Hu, Y. Wang, T. Ou, M. L. Povinelli, W. Wu, Effects of roughness and resonant-mode engineering in all-dielectric metasurfaces, *Nanophotonics* 9 (2020) 1401–1410.
- [33] S. Sun, Z. Zhou, C. Zhang, Y. Gao, Z. Duan, S. Xiao, Q. Song, All-dielectric full-color printing with TiO₂ metasurfaces, *ACS Nano* 11 (2017) 4445–4452.
- [34] H. Hsiao, C.H. Chu, D.P. Tsai, Fundamentals and applications of metasurfaces, *Small Methods* 1 (2017), 1600064.
- [35] R. Fu, Z. Li, G. Zheng, M. Chen, Y. Yang, J. Tao, L. Wu, Q. Deng, Reconfigurable step-zoom metalens without optical and mechanical compensations, *Opt. Express* 27 (2019) 12221–12230.
- [36] S. Tian, H. Guo, J. Hu, S. Zhuang, Dielectric longitudinal bifocal metalens with adjustable intensity and high focusing efficiency, *Opt. Express* 27 (2019) 680–688.
- [37] X. Zang, H. Ding, Y. Intaravanne, L. Chen, Y. Peng, J. Xie, Q. Ke, A.V. Balakin, A. P. Shkurinov, X. Chen, Y. Zhu, S. Zhuang, A multi-foci metalens with polarization-rotated focal points, *Laser Photon. Rev.* 13 (2019), 1900182.
- [38] K. Guo, H. Xu, Z. Peng, X. Liu, Z. Guo, High-efficiency full-vector polarization analyzer based on GaN metasurface, *IEEE Sens. J.* 19 (2019) 3654–3659.
- [39] J. Wang, J. Ma, Z. Shu, Z. Hu, X. Wu, Terahertz metalens for multifocusing bidirectional arrangement in different dimensions, *IEEE Photon. J.* 11 (2019) 1–11.